L. De Siena and A. Amoruso contributed equally to this work.

Key Points:
- Advanced deformation analysis detects environmental components linked to seismic migrations and variations in carbon dioxide fluxes
- A wet hydrological year during a drought closed Solfatara, increasing pressure and breaking the shallow caldera in early 2018
- The deep unrest sources cracked the weakened eastern caldera in 2018–2019, causing seismic unrest

Author Contributions:

Conceptualization: L. De Siena, A. Amoruso, S. Petrosino, L. Crescentini
Data curation: L. De Siena, A. Amoruso, S. Petrosino, L. Crescentini
Formal analysis: A. Amoruso, L. Crescentini
Investigation: L. De Siena, A. Amoruso, L. Crescentini
Methodology: A. Amoruso, L. Crescentini
Software: L. De Siena, A. Amoruso, L. Crescentini
Validation: L. De Siena, A. Amoruso, S. Petrosino, L. Crescentini
Visualization: L. De Siena
Writing – original draft: L. De Siena

Geophysical Responses to an Environmentally-Boosted Volcanic Unrest

L. De Siena[1,2,3] ![ORCID], A. Amoruso[4] ![ORCID], S. Petrosino[5] ![ORCID], and L. Crescentini[4] ![ORCID]

[1]Institute of Geosciences, Johannes Gutenberg University, Mainz, Germany, [2]TeMaS—Terrestrial Magmatic Systems Research Area, Johannes Gutenberg University, Mainz, Germany, [3]Department of Physics and Astronomy "Augusto Righi", Alma Mater Studiorum, Bologna, Italy, [4]Department of Physics, University of Salerno, Fisciano, Italy, [5]Istituto Nazionale di Geofisica e Vulcanologia, Sezione di Napoli—Osservatorio Vesuviano, Napoli, Italy

Abstract The spatiotemporal relationship between geophysical, environmental, and geochemical responses during volcanic unrest is essentially unknown, making their joint use and interpretation for eruption forecasting challenging. Here, Empirical Orthogonal Functions analysis applied to GPS data allows the separation of the dominant deep-sourced inflation from environmentally controlled signals associated with extension at Campi Flegrei caldera. This separation bridges the gap between deformation, seismic and geochemical responses, clarifying the processes underlying the ongoing volcanic unrest. Persistent meteoric forcing during the 2017–2018 hydrological year changed the decadal trend of seismic energy and secondary deformation components, pairing their spatial patterns. The result was a block in the carbon dioxide released in 2018 at Solfatara, the primary stress-release valve at the caldera. The subsequent overpressure weakened the fractured eastern caldera, opening pathways for deep, hot materials to reach the surface. Our results give insight into how environmental forcing can favor volcanic unrest in pressurized calderas.

Plain Language Summary Geophysics and geochemistry are two of the most essential disciplines to understand volcanic unrest and eruptions. Finding the link between deformation signals and their seismic and geochemical counterparts is crucial in understanding how a volcano works; however, a time-resolved 3D analysis of signals sensitive to different processes, from magma migration to environmental forcing, is our best chance to understand how the volcano changes and when an eruption might occur. We borrowed standard oceanic and climatic data analysis techniques and applied them to GPS signals recorded during unrest at Campi Flegrei caldera. The results uncovered small deformation components linked to seismic migrations and variations in carbon dioxide fluxes measured at the Solfatara crater. These components clarify how a drought can weaken the shallowest crust, strengthening ongoing processes generated at depth. A wet hydrological year in the middle of the ongoing drought coincided with decreased emissions of carbon-bearing fluids from Solfatara, the primary stress-release valve of the caldera. This stress was eventually released when deep materials rose in the eastern caldera, producing seismicity. Highlighting small components in deformation signals linked to environmental changes appears essential to mark variations in volcanic behavior, in analogy to what is done by ambient noise interferometry.

1. Introduction

The method of Empirical Orthogonal Functions (MEOF), a powerful tool for weather forecasting (Lorenz, 1956) and climate and oceanic modeling (Hannachi et al., 2007; Navarra & Simoncini, 2010; Smith et al., 1996), is equivalent to a Principal Component Analysis applied to data that have a combination of spatial and temporal trends (Zerbini et al., 2013). MEOF decomposes a space-time field into spatial patterns and associated time indices, where the components reflect different but interconnected processes (Navarra & Simoncini, 2010). When applied to GPS data at the continental scale over a decade, the main EOF components reveal environmental forcing associated with a hot, dry season (Zerbini et al., 2013). Its application to InSAR data at Campi Flegrei caldera (Southern Italy, Figures 1a and 1b) shows that the first EOF component captures most of the deformation signal and can be modeled as the response to magma or magmatic fluid inflation, producing unrest at least since 2015 (Amoruso & Crescentini, 2022). In a volcano, transient magmatic, geochemical, and environmental processes are tightly entangled; it is thus essential to analyze components other than the first, as they might have a higher sensitivity to such transients (Monahan et al., 2009).

Carbon-bearing subsurface fluids are the primary cause of surficial volcanic activity at Campi Flegrei (Siniscalchi et al., 2019). These fluids could come from decarbonation reactions (Vanorio & Kanitpanyacharoen, 2015) or a hot fluid reservoir of debated magmatic origin at a depth of ~3.5 km (red ellipses, Figures 1a—Amoruso,
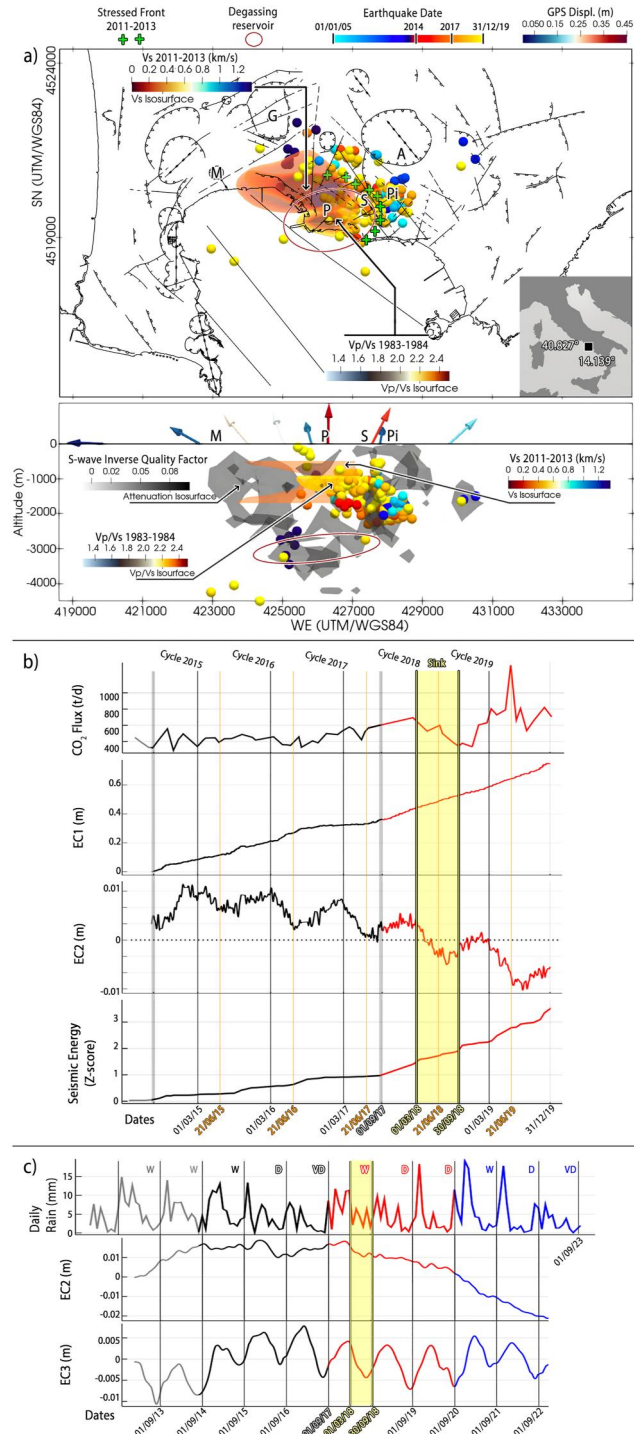

Figure 1.

Crescentini, & Sabbetta, 2014; Amoruso, Crescentini, Sabbetta, et al., 2014; Amoruso et al., 2015, 2017; Buono et al., 2022; Castaldo et al., 2021) or ~8 km (Moretti et al., 2018). The ~3.5-km-deep hot reservoir sits under a deforming caprock (Calò & Tramelli, 2018; De Siena, Amoruso, et al., 2017; De Siena, Chiodini, et al., 2017; Vanorio & Kanitpanyacharoen, 2015). It feeds (a) a ~1 km-deep reservoir active in 1983–1984 (yellow isosurface, Figures 1a—Vanorio et al., 2005); (b) high-attenuation fluids (gray isosurface, Figures 1a—De Siena, Chiodini, et al., 2017) to the Solfatara (**S**) vent and Monte Nuovo (**M**) area.

Campi Flegrei appears as a prototypical geothermal system (Lu, 2018) where high-pressure fluid injections from depth open pre-existing fractures in shallower rock formations (De Siena, Amoruso, et al., 2017; De Siena, Chiodini, et al., 2017). These injections increase stress and heat in the 1983–1984 reservoir, creating a stressed front (Nespoli et al., 2021—Figure 1a, plus symbols (+) from Pepe et al., 2019 mapped using InSAR measurements between 2012 and 2014) intersecting the pathway followed by migrating fluids outgassing and overflowing the eastern caldera-bounding faults (Petrosino & De Siena, 2021; Siniscalchi et al., 2019). By the end of 2013, the 1983–1984 reservoir had expanded aseismically (Di Luccio et al., 2015), reaching the northern portion of the caldera rim (orange isosurface, Figures 1a, De Siena et al., 2018). Between 2005 and 2014, seismic energy increased via extensional swarms lasting a few days (Tramelli et al., 2022). Environmental forcings like excessive rainfalls (Petrosino et al., 2021; Scafetta & Mazzarella, 2021) and tides (Petrosino & Dumont, 2022; Petrosino et al., 2018) can transform such an over-pressurized system (Kilburn et al., 2017) in an enhanced geothermal system (Lu, 2018).

Forcing similar to that observed at the continental scale (Zerbini et al., 2013) was most likely active during the 2017–2018 wet hydrological year (Table S1 in Supporting Information S1) when anomalous continuous precipitations hit the caldera during the strongest drought of the decade (2015–2020—Figure 1c). Deeper magmatic reservoirs are primary contributors to seismicity at Campi Flegrei; however, seismic energy (Tramelli et al., 2021; Figure 1b and Figure S1 in Supporting Information S1) steepens after July 2014 (from gray to black seismic energy trend) and more clearly in September 2017 (from black to red, Figure S1 in Supporting Information S1). Short-range (from hours to days) seismic rates and intensities are tied to external modulators like tides and precipitations (Hainzl et al., 2006; Matthews et al., 2009; Neuberg, 2000) in such pressurized hydro-geothermal systems (Petrosino & De Siena, 2021; Scafetta & Mazzarella, 2021). Carbon dioxide (CO_2) emissions at Solfatara and its faults (Bruno et al., 2007; Di Martino et al., 2022, **S**—Figures 1b, 2a, and 3a) are primary manifestations of the Campi Flegrei unrest. The second portion of the 2017–2018 hydrological year (February-September) also corresponds to the longest and largest CO_2 flux sink ever recorded at Solfatara (Figures 1b and 1c and Figure S1 in Supporting Information S1).

The relationship between deformation and rainfall is more ambiguous (Petrosino et al., 2021). Raw GPS signals show variations that are difficult to link to coeval geochemical and seismic signals across the whole caldera and are primarily associated with deep-sourced carbon or magma throughout the 2005–2019 unrest (Amoruso & Crescentini, 2022; Amoruso et al., 2015; Moretti et al., 2018; Vanorio & Kanitpanyacharoen, 2015). The injection of meteoric fluids likely leads to thermo-poroelastic processes (Moretti et al., 2018; Nespoli et al., 2021; Scafetta & Mazzarella, 2021), but separating the deformation signals produced by deep and shallow processes and linking them to seismicity remains challenging. However, the anomalous continuous precipitations in the middle of the 2015–2020 drought (Figure 1c) represent a long-range environmental forcing that the MEOF can detect (Zerbini

Figure 1. Geomorphology, seismicity, deformation, and geochemistry at Campi Flegrei. (a) The geomorphological and structural map of the caldera (Isaia et al., 2015; Vilardo et al., 2007) is superimposed on the yellow and orange isosurfaces representing high-V_p/V_s (1983–1984—Vanorio et al., 2005) and low-velocity (2011–2013—De Siena et al., 2018) anomalies, respectively. The bottom of the high-attenuation isosurface (gray, 1983–1984) coincides with a hot inflating and degassing reservoir (Buono et al., 2022; Castaldo et al., 2021). Green symbols (+, Pepe et al., 2019): seismic front of the thermo-poroelastic reservoir in 2012–2014. Colored circles: earthquakes above magnitude 0.75 color-coded by nucleation time. **P** = Pozzuoli; **S** = Solfatara; **Pi** = Pisciarelli; **M** = Monte Nuovo; **A** = Astroni; **G** = Gauro. Arrows at the surface: GPS displacement directions and total uplift on 31 December 2019 (De Martino et al., 2021). (b) From top to bottom, the temporal relation between soil CO_2 flux at Solfatara (Chiodini et al., 2021), *EC1*, *EC2*, and *Z*-score (seismic energy, Tramelli et al., 2021) from 22 July 2014 to December 2019. Changes from gray to black to red in the time series correspond to three different seismic energy trends associated with varying seismic swarm durations (see Figure S1 in Supporting Information S1). Yellow bars and dates highlight the 2018 sink (1 March–29 September). Thin black and orange lines mark 01/03 and 21/06 every year, respectively. (c) From top to bottom, the temporal relation between average daily precipitations over a month, and EC2 and EC3 calculated from weekly GPS data extending to December 2022 (De Martino et al., 2023). Black vertical lines represent the start of a hydrological year. The blue-colored lines show trends from 1 September 2020, onwards. Dry (D), Very Dry (VD), and Wet (W) years are reported with precipitations and defined following Table S1 in Supporting Information S1.
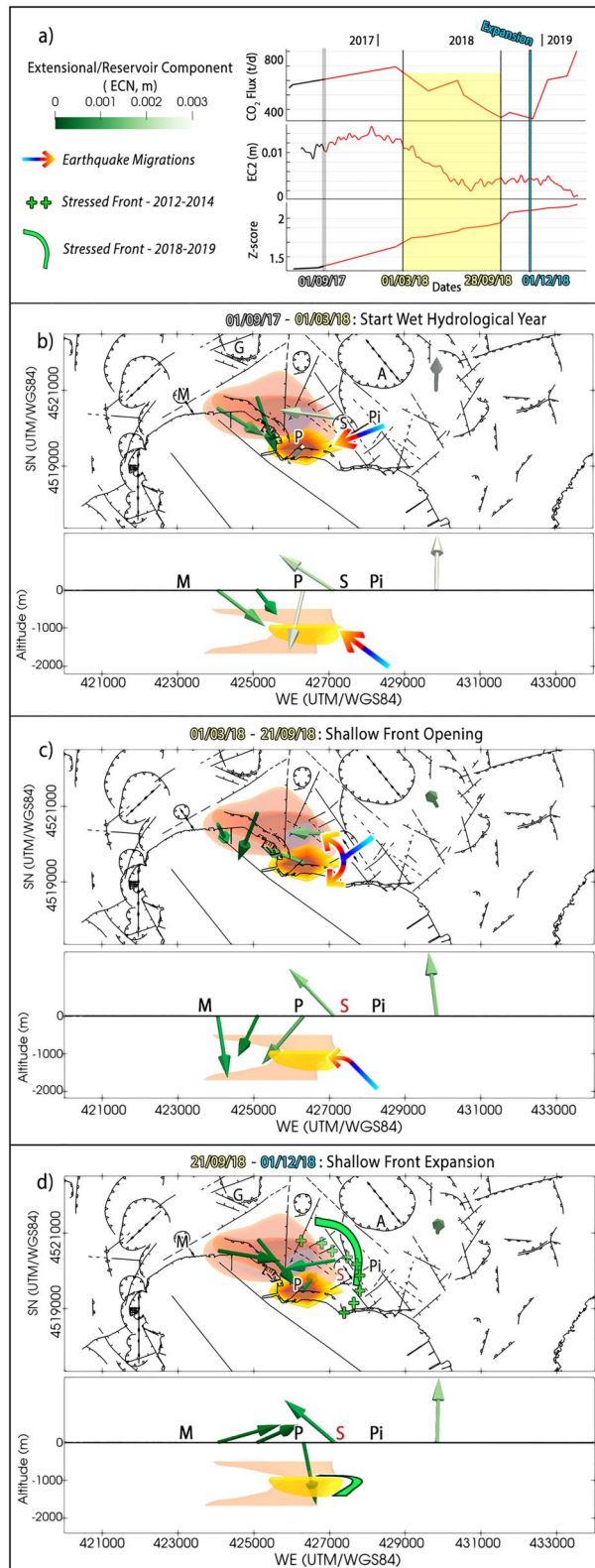
Figure 2.

et al., 2013) once applied to daily GPS data within the caldera (Figure 1a, GPS measurements, De Martino et al., 2021).

This study uses the MEOF to identify deep-sourced and environmental processes underlying the GPS deformation field. It shows that secondary deformation patterns linked to environmental forcing pair with seismic migrations, while their temporal components detect the closure of the primary stress-relief valve at Campi Flegrei: outgassing at Solfatara. Because of the subsequent shallow overpressure, a long-lived front (Pepe et al., 2019) expanded east, widening the fumarolic field at Pisciarelli (Fedele et al., 2020) and breaking the weakened crust in 2019, boosting the ongoing deep-sourced unrest.

2. Methods

2.1. Empirical Orthogonal Functions

GPS displacements (North, East, and Up) measured across the caldera are arranged in a data matrix X having as many columns as the number of GPS stations multiplied by the number of the displacement components (three) and as many rows as the number t of measurement times. We limit our analysis to co-recording stations having no extended gaps (Figure S2a in Supporting Information S1 shows stations used from 2013/2014 and 2016). By singular value decomposition, we obtain:

$$X = U \times D \times V^T = EC \times EOF^T. \tag{1}$$

U and V are orthonormal, D is diagonal, $EC = U \times D$, and $EOF = V$. The columns EC (Expansion Coefficients—Navarra & Simoncini, 2010) give the temporal patterns; the columns of the matrix EOF give the (mutually orthogonal) spatial patterns. We thus associate a temporal (ECn) and a spatial (EOFn) pattern to each component n at each station. The relevance of both patterns depends on the diagonal elements in matrix D or (as more commonly presented) on $\Lambda_k = \lambda_k^2$, the covariance matrix (Figure S2b in Supporting Information S1). We estimate a component significance from the eigenvalue errors, given as Λ_k sqrt($2/p$), where p is the number of statistically independent samples (Navarra & Simoncini, 2010) calculated using the autocorrelation function (Thiiébaux & Zwiers, 1984). Usually, few components capture most of the original information; however, the need for spatial orthogonality, temporal uncorrelation, and nonlocal maximization of variance over the domain in different components implies that each component has no dynamical, kinematic, and statistical meaning independently of the others (Monahan et al., 2009).

A quasi-linear trend induced by the Campi Flegrei uplift dominates the GPS time series; thus, we first compute the autocorrelation function of X to estimate p for EC1; then, we estimate p for the other components combined (i.e., ECN) by computing the autocorrelation for a matrix obtained by subtracting EC1 from X. We noted an unrealistic correlation between specific temporal variations of EC1 and EC2 at all stations of the caldera (Figure S4 in Supporting Information S1). This effect is probably due to the slight high-frequency movement (noise) of the reference GPS stations. We thus analyzed *displacement-removed* data: we removed the mean of each displacement component over n_r stations outside the caldera from each row in X (i.e., at each time). The displacements of the external stations are arranged in a data matrix R having n_t rows and $3n_r$ columns. For each $X_{i,j}$, we compute $k = j\%3$ (% is the modulo operator, and $k = 3$ if $j\%3 = 0$). The elements of the displacement-removed data matrix Y are:

$$Y_{i,j} = X_{i,j} - (\Sigma_{m=1,nr} R_{i,3(m-1)+k})/n_r. \tag{2}$$

2.2. Earthquake Locations

The Campi Flegrei seismicity is monitored by the permanent and mobile seismic networks of Istituto Nazionale di Geofisica e Vulcanologia, Sezione di Napoli—Osservatorio Vesuviano (INGV-OV). The data set consists of

Figure 2. Seismic and secondary deformation patterns before and during the sink. (a) CO_2 soil flux, EC2, and seismic energy time series from the 2017 rainfall events (Scafetta & Mazzarella, 2021) to the end of the sink. Line colors are identical to those in Figure 1b. Green color scale: ECN average deformation in each period. (b–d) Comparison between the EOFN and ECN patterns (arrows at the surface and their color), interpreted seismic migrations (arrows color-coded like earthquakes in Figures S6b–S6d in Supporting Information S1) and fronts. Solfatara (**S**) is labeled in red during sink periods and otherwise black.
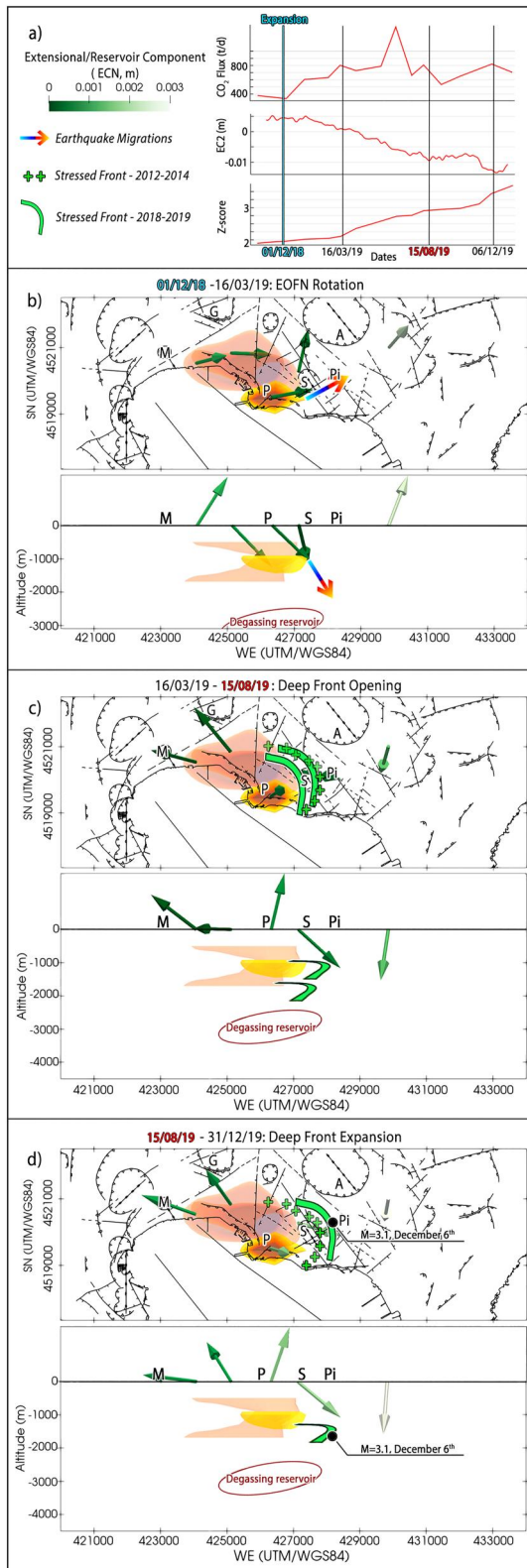
Figure 3. Seismic and secondary deformation patterns after the sink. Same as Figure 2 for the recovery period from the sink to the end of 2019. The arrows showing seismic migrations are color-coded like earthquakes in Figures S7b–S7d in Supporting Information S1.

volcano-tectonic earthquakes detected in 2005–2019 (color-coded circles, Figure 1a). *P*- and *S*-phases recorded by the networks were picked, integrated, and inverted with a probabilistic non-linear 3D grid search. We used the NLLOC software (Lomax et al., 2014) to search for the best solution within the 3D velocity structure of Battaglia et al. (2008). Locations with RMS higher than 0.1 were removed from the data set.

3. Results

3.1. Deformation Modes and Joint Spatial Analysis

We apply the MEOF to deformation signals recorded until December 2019: (a) from January 2013, (b) from July 2014, and (c) from July 2016 (see Text S1 in Supporting Information S1). In all cases and independently of processing: (a) EC1 explains >98.9% of the variance (Figure S2b in Supporting Information S1); (b) EOF1 patterns correspond to the inflation of deformation sources in the center of the caldera (Figure S2a, arrows in Supporting Information S1), analogue to the one obtained using InSAR data (Amoruso & Crescentini, 2022). The dependence of GPS data on inflation means that few samples are independent when including EC1, which is always statistically significant (Figure S2b in Supporting Information S1). The autocorrelation computed on ECN shows that only EC2 is statistically significant (insets in Figure S2b in Supporting Information S1). The displacement-removed processing drastically reduces noise on EC1 and its correlations with EC2 (Figure S5 in Supporting Information S1).

From now on, we will always refer to displacement-removed components. EC2 is our primary proxy for the time variation of components different from EC1 due to its statistical significance and contribution to the variance (Figure S2b in Supporting Information S1). It shows similar oscillatory behaviors in all periods considered, independently from differences in station numbers (Figure 1b, Figure S2c in Supporting Information S1). EOF1 shows inflation with a maximum at the center of the 1983–1984 reservoir in all periods (Figure S2a in Supporting Information S1). It is almost identical to the GPS pattern (Figure 1a). From 2015, EC2 shows an annual cycle (Figure 1b) comprising a decrease from the start of March (black vertical lines) to 21 June (orange lines), a plateau through the summer, and an increase from September to the end of February (black and red curved arrows in Figure 1b). The only years with no plateau are 2018 and 2019, with a decrease lasting ~1 and ~2 months longer (Figure 1b) followed by a sudden increase during the sink. We also show EC2 calculated from 2016 with seismic energy around the period of CO_2 sink in 2018 (Figure 2a) and during the subsequent seismic unrest (Figure 3a).

Figures 2b–2d and 3b–3d show jointly:

1. The summed spatial pattern of the displacement of all components except the first (EOFN, arrows, also named Extensional/Reservoir component) for stations inside the caldera rim. The associated green and white color scale shows the average ECN displacement over the same period. Figures S3b–S3g in Supporting Information S1 shows ECN and EOFN at all stations used in the same periods.
2. Earthquake migrations (color-coded arrow) and fronts (green curves) defined from earthquake locations (circles, Figures S6 and S7 in Supporting Information S1) spanning the same period. In Figures 2 and 3, locations and interpreted migrations are labeled using the same color scale (cyan = oldest;

yellow = youngest). A seismic front appears when seismicity consistently distributes across a volume without an apparent temporal trend.

3.2. Comparison Between Temporal Trends

Scafetta and Mazzarella (2021) show that a 7–11 September 2017 extreme rain event (>200 mm of meteoric water over 4 days, twice the total amount of an average September) follows a ∼2-year gap in the correlation between seismic swarms and rainfall, corresponding to a 2-year drought (Figure 1c). At the beginning of 2019, the CO_2 flux recovered the exponential trend followed before the sink. EC1 and EC2 show no apparent relation to these rainfall events, with our processing removing the minor, transient increases at both ends of the sink (Figure S5 in Supporting Information S1, EC1 and EC2). The 2018 cycle coincides with the beginning of the CO_2 sink (1 March 2018, Figures 1c and 2a). The 2019 seasonal EC2 decrease comprises the maximum CO_2 flux measured at Solfatara until 2019 (Figure 1c); if calculated from 2016, the 2019 decrease ended in August (Figure 3a), ∼2 months later than in 2016 and 2017, which suggests a primary change in the behavior of the EC2 time series hidden by its seasonal oscillations.

4. Discussion

4.1. Deformation and Seismic Responses to a Carbon Sink

Deep deformation sources have been active since at least 2015 at the caldera and are controlling EC1 (Amoruso & Crescentini, 2022). The September 2017 events were the first manifestation of some of the highest (Table S1 in Supporting Information S1) and most continuous yearly precipitations recorded since 2012 at the caldera (Figure 1c). They happened in the middle of a 5-year drought, which, at the continental scale, controls EOF components (Zerbini et al., 2013). EC2 thus appears to be a significant marker of year-long environmental and seasonal processes alternative to deep-sourced deformation. However, it must be considered with additional components to infer their dynamical, kinematic, and statistical meaning. Hence, we compare their combined spatial (EOFN—arrows) and temporal (the ECN color scale shows the average displacement over the period) patterns with coeval seismic migrations and fronts in Figures 2b–2d and 3b–3d (see ECN and EOFN across the entire caldera in Figure S3 in Supporting Information S1).

In the 5 months before the sink, earthquakes consistently migrated from NE (Pisciarelli) to SW across the SW-to-NE-striking fault crossing Solfatara (color-coded arrow, Figure 2b). Seismic activity on this fault has been a primary stress-release valve at the caldera since the unrest started, in 2005 (Bruno et al., 2007; Chiodini et al., 2021; Isaia et al., 2015; Vilardo et al., 2007). The fault remains the only seismically active, degassing connection between the expanding central reservoirs and a critically stressed front, contouring the eastern reservoir boundary between 2012 and 2014 (Pepe et al., 2019—Figure 2d, green + symbols). Right before the sink, these migrations were associated with compression of the 1983–1984 reservoir (ECN sinks into the reservoir, Figure 2b), while the stress from deeper sources increased at a higher rate (EC1, Figure 1c). The EC2 pattern points to a compression of the 1983–1984 supercritical fluid reservoir, which coupled with the extensional mechanics (Tramelli et al., 2022) responding to inflation and deflation from the deep, hot reservoir (Amoruso & Crescentini, 2022).

The shallow (∼1 km depth) volumes under the Solfatara fault remain aseismic throughout the sink and right after it (Figures S6c and S6d in Supporting Information S1, red **S**). Solfatara presents a clay cap with few faults, allowing fluid migration (Bruno et al., 2007; Isaia et al., 2015; Siniscalchi et al., 2019; Vilardo et al., 2007). Increased pore pressure from the 2017–2018 precipitations, following the much dryer 2016–2017, can increase permeability across the cap by opening cracks and pores; however, progressive increases in pore pressure dislodge clay minerals and impede the flow from depth (e.g., Coyner, 1977) so that the cap becomes a *plug* in the carbon flow (Figure 2a), increasing stress as the system dries up in the summer (Moretti et al., 2018). This process is enhanced by thermal expansion and liquefaction (Chiodini et al., 2021; Siniscalchi et al., 2019), which further lower the ability of rocks to fracture, producing earthquakes. While the relation between gas emissions at Solfatara and Pisciarelli was unclear before the sink, their time series were anticorrelated during the sink (Figure S8 in Supporting Information S1). The plug caused earthquakes to plateau at ∼1 km under Solfatara while seismic fluids migrated toward Pisciarelli (Figure 2c) through communicating aquifers (Isaia et al., 2022). During the sink, CO_2-bearing fluids could only surface near the Pisciarelli vent, where the clay cap had not formed (Siniscalchi et al., 2019), drastically increasing the corresponding emissions.

The relationship between EOFN, seismic patterns, and reservoir locations clarifies how the system released the combined stress from the plugged Solfatara and the deep inflating sources at the end of the sink. During the sink, seismic migrations rose from Pisciarelli. They contoured the 1983–1984 reservoir (Figure 2c, splitting color-coded arrows, maximum earthquake depths at 2.3 km), defining its eastern 2012–2014 front (Nespoli et al., 2021; Pepe et al., 2019). This seismic behavior is typical of stress release from an over-pressurized thermo-poro-elastic reservoir, specifically of the opening of its shallow crustal front (Lu, 2018; Nespoli et al., 2021). The 2011–2013 low-velocity reservoir was depressurized in 2018 (Petrosino & De Siena, 2021), storing fluids that migrated toward the east. On the contrary, the 1983–1984 supercritical fluid reservoir remained aseismic and coincided with the area of highest pressurization throughout the unrest (Petrosino & De Siena, 2021).

The result of the opening at the top of the system was the definition of a new seismically active front at the end of 2018, further north and east of the central supercritical fluid reservoirs (Figure 2d, green curve), which released stress and stopped the CO_2 flux sink (Figure 2a). Right after the sink, seismic patterns distributed much further east and north than the pre-existing front (+symbols, Figure S6d in Supporting Information S1), almost reaching the Astroni crater. In the same period, the EOFN started rotating toward the east with the corresponding ECN (color scale) lower than during the sink (see Figures 2b–2d), a signal of the incoming predominance of deep-sourced processes. The shift of the seismic front and the start of a clockwise rotation of the ECN are a symptom of the incoming extensional dynamics that will produce the highest-magnitude earthquakes at the caldera since 1984 (Tramelli et al., 2022).

4.2. Top-Down Control on Stress Release Contributes to Unrest

The opening of the shallow front was a vital contributor to the 2019 unrest, characterized by excessive outgassing (Figure 3a) and the highest seismic and deformation rates recorded since 1984 (Chiodini et al., 2021). Recovery from the sink corresponded with the re-establishment of seismic migrations from the caldera center to Pisciarelli across the Solfatara fault, coeval to the release of extensional stress from the 1983–1984 reservoir (Figure 3b, color-coded arrow). From this point onwards, EC2 and seismic energy followed opposite linear trends (Figure 3a) until the 3.1 Md event of 6 December 2019. The ECN spatial patterns had fully rotated east (Figure 3b), imaging expansion of the central reservoir associated with co-directed, downward seismic migrations. We infer that ECN and seismic migrations are proxies for extensional dynamics, with their patterns opposite to those at the start of the sink. They show (a) the close link between secondary EC components and the release of seismic energy and (b) how opposite geophysical responses characterize geochemical sink and recovery.

The Solfatara plugging and associated liquefaction and thermo-elastic processes (Scafetta & Mazzarella, 2021; Siniscalchi et al., 2019) had weakened the shallow portion of the caldera east of the supercritical reservoir in 2018, but seismic migrations had only cracked the eastern boundary of the shallow reservoir and opened a shallow front. In 2019, the result of this shallow caldera staging (Roman & Cashman, 2018) was (a) the rise of materials from the deep degassing reservoir to the eastern tip of the main SW-NE striking fault at Solfatara and (b) the seismic opening of the SN pressurized transfer structure connecting Pozzuoli and Astroni and acting as new seismic front (Figure 3b, green curve—Petrosino & De Siena, 2021). The recovery of the CO_2 flux coincided with consistent seismic migrations east of the front opened at least since 2014 (+symbols, Figure S9 in Supporting Information S1), which will generate the highest-magnitude earthquakes since 1984 at the caldera. ECN patterns in this period pointed to the deep, hot source of unrest right below Pozzuoli, opening a deeper seismic front (Figure 3c) in the eastern caldera and beyond. The mechanisms acting before 2017–2018 could not sustain the corresponding stress, leading to higher seismic rates in 2019 (Tramelli et al., 2021). The EC1 rates are the strongest across our data set. In this period, the new seismic front expanded east, while EOFN points to the volumes associated with the highest-magnitude earthquakes (Figures 3d, Tramelli et al., 2021).

On 8 November 2023, weekly GPS data extending to November 2022 were released (De Martino et al., 2023), allowing us to process data over the same array of stations, even if at a lower time resolution. The MOEF effectively separates the long-range environmental and extensional behavior (EC2, Figure 1c) previously hidden under the oscillatory short-range seasonal forcing (EC3, Figure 1c): these two components are the primary contributors to the EOFN patterns, spatially coupled with seismic migrations and fronts (Figures 2 and 3). The two leading secondary EOF components (Figure S10 in Supporting Information S1) thus depend on environmental forcing, with the EC2 stress release (decrease) starting after the sink at Solfatara, that is, at the end of the 2017–2018 wet hydrological year (Figure 1c). This is when EOFN patterns rotate while seismicity marks a shallow front

expansion (Figures 2c and 3a), the turning point for deep materials to rise to the surface (Figures 3b–3d). A stronger decrease characterizes EC2 around the start of the wet 2020–2021 hydrological year (Figure 1c, blue), but the lower temporal resolution of GPS data forbids a joint spatial analysis with seismicity. Our results suggest it is possible to detect changes leading to seismic unrest in the eastern caldera from geochemical (CO_2 sink, Figure 1b) and secondary deformation (Figure 1c, EC2) time series. Analyzing decadal daily GPS recordings could lead to more accurate forecasts and clarify the contribution of seasonal and decadal environmental effects on deformation data.

5. Conclusions

This study represents the first joint analysis of Empirical Orthogonal Functions applied to GPS data, time-lapse earthquake migrations and CO_2 flux time series. Its results show the geophysical time-resolved response to environmental and deep processes producing unrest at a volcanic caldera—an image of how the volcano responds to being increasingly stressed from depth and surface. The caldera momentarily reduces its carbon outflow, storing rising carbon-bearing fluids within its eastern faults. This storage becomes an additional pressure source that can further crack the shallow fractured eastern caldera around expanding thermo-poroelastic supercritical fluid reservoirs, opening a pathway for deeper materials to rise to the surface.

The relationships between the 1983–1984 supercritical fluid reservoir, the ECN and EOFN secondary deformation patterns, and seismic migrations show that extensional processes associated with fluid migrations are a vital release valve for increases in thermo-poroelastic stress primarily caused by deep degassing sources. Increased shallow carbon storage and year-long environmental forcing can perturb this cyclic stress release mechanism. Our study suggests that continuous long-lasting meteoric forcing amid extended periods of drought contributes to geophysical and geochemical responses primarily controlled by deep processes: understanding this forcing appears central to assessing volcanic hazards at this and other volcanic calderas.

Data Availability Statement

This study uses routine seismic picks performed by the staff of the seismic laboratory at the INGV-OV. Rainfall (amount) data were downloaded from the 3Bmeteo (2023) portal, which provides historical rainfall data for Pozzuoli. Giuseppe Vilardo provided the ESRI shapefiles used to plot faults and fractures. The ASCII files corresponding to the seismic and MEOF analyses necessary to reproduce results and figures have been deposited in the Open Science Framework database (De Siena et al., 2023). The final figure layouts were prepared using Photoshop CS©.

References

3Bmeteo. (2023). Dati Meteo Storici [Dataset]. 3Bmeteo. Retrieved from https://www.3bmeteo.com/meteo/pozzuoli/storico

Amoruso, A., & Crescentini, L. (2022). Clues of ongoing deep magma inflation at Campi Flegrei caldera (Italy) from empirical orthogonal function analysis of SAR data. *Remote Sensing*, *14*(22), 5698. https://doi.org/10.3390/rs14225698

Amoruso, A., Crescentini, L., D'Antonio, M., & Acocella, V. (2017). Thermally-assisted magma emplacement explains restless calderas. *Scientific Reports*, *7*(1), 7948. https://doi.org/10.1038/s41598-017-08638-y

Amoruso, A., Crescentini, L., & Sabbetta, I. (2014). Paired deformation sources of the Campi Flegrei caldera (Italy) required by recent (1980–2010) deformation history. *Journal of Geophysical Research: Solid Earth*, *119*(2), 858–879. https://doi.org/10.1002/2013jb010392

Amoruso, A., Crescentini, L., Sabbetta, I., De Martino, P., Obrizzo, F., & Tammaro, U. (2014). Clues to the cause of the 2011–2013 Campi Flegrei caldera unrest, Italy, from continuous GPS data. *Geophysical Research Letters*, *41*(9), 3081–3088. https://doi.org/10.1002/2014gl059539

Amoruso, A., Crescentini, L., Scarpa, R., Bilham, R., Linde, A. T., & Sacks, I. S. (2015). Abrupt magma chamber contraction and microseismicity at Campi Flegrei, Italy: Cause and effect determined from strainmeters and tiltmeters. *Journal of Geophysical Research: Solid Earth*, *120*(8), 5467–5478. https://doi.org/10.1002/2015jb012085

Battaglia, J., Zollo, A., Virieux, J., & Iacono, D. D. (2008). Merging active and passive data sets in traveltime tomography: The case study of Campi Flegrei caldera (southern Italy). *Geophysical Prospecting*, *56*(4), 555–573. https://doi.org/10.1111/j.1365-2478.2007.00687.x

Bruno, P. P. G., Ricciardi, G. P., Petrillo, Z., Di Fiore, V., Troiano, A., & Chiodini, G. (2007). Geophysical and hydrogeological experiments from a shallow hydrothermal system at Solfatara Volcano, Campi Flegrei, Italy: Response to caldera unrest. *Journal of Geophysical Research*, *112*(B6), 74. https://doi.org/10.1029/2006jb004383

Buono, G., Paonita, A., Pappalardo, L., Caliro, S., Tramelli, A., & Chiodini, G. (2022). New insights into the recent magma dynamics under Campi Flegrei caldera (Italy) from petrological and geochemical evidence. *Journal of Geophysical Research: Solid Earth*, *127*(3), e2021JB023773. https://doi.org/10.1029/2021jb023773

Calò, M., & Tramelli, A. (2018). Anatomy of the Campi Flegrei caldera using enhanced seismic tomography models. *Scientific Reports*, *8*(1), 1–12. https://doi.org/10.1038/s41598-018-34456-x

Castaldo, R., Tizzani, P., & Solaro, G. (2021). Inflating source imaging and stress/strain field analysis at Campi Flegrei caldera: The 2009–2013 unrest episode. *Remote Sensing*, *13*(12), 2298. https://doi.org/10.3390/rs13122298

Chiodini, G., Caliro, S., Avino, R., Bini, G., Giudicepietro, F., De Cesare, W., et al. (2021). Hydrothermal pressure-temperature control on CO_2 emissions and seismicity at Campi Flegrei (Italy). *Journal of Volcanology and Geothermal Research*, *414*, 107245. https://doi.org/10.1016/j.jvolgeores.2021.107245

Coyner, K. (1977). *Effects of stress, pore pressure, and pore fluids in bulk strain, velocity, and permeability in rocks, PhD Dissertation*. MIT.

De Martino, P., Dolce, M., Brandi, G., & Scarpato, G. (2023). Campi Flegrei cGPS weekly positions time series [Dataset]. Zenodo. https://doi.org/10.5281/zenodo.10082465

De Martino, P., Dolce, M., Brandi, G., Scarpato, G., & Tammaro, U. (2021). The ground deformation history of the neapolitan volcanic area (Campi Flegrei caldera, Somma–Vesuvius Volcano, and Ischia island) from 20 years of continuous GPS observations (2000–2019). *Remote Sensing*, *13*(14), 2725. https://doi.org/10.3390/rs13142725

De Siena, L., Amoruso, A., Petrosino, S., & Crescentini, L. (2023). Geophysical responses to an environmentally-boosted volcanic unrest [Dataset]. OSF. https://doi.org/10.17605/OSF.IO/EFC28

De Siena, L., Amoruso, A., Pezzo, E. D., Wakeford, Z., Castellano, M., & Crescentini, L. (2017). Space-weighted seismic attenuation mapping of the aseismic source of Campi Flegrei 1983–1984 unrest. *Geophysical Research Letters*, *44*(4), 1740–1748. https://doi.org/10.1002/2017gl072507

De Siena, L., Chiodini, G., Vilardo, G., Del Pezzo, E., Castellano, M., Colombelli, S., & Ventura, G. (2017). Source and dynamics of a volcanic caldera unrest: Campi Flegrei, 1983–84. *Scientific Reports*, *7*(1), 1–13. https://doi.org/10.1038/s41598-017-08192-7

De Siena, L., Sammarco, C., Cornwell, D. G., La Rocca, M., Bianco, F., Zaccarelli, L., & Nakahara, H. (2018). Ambient seismic noise image of the structurally controlled heat and fluid feeder pathway at Campi Flegrei caldera. *Geophysical Research Letters*, *45*(13), 6428–6436. https://doi.org/10.1029/2018gl078817

Di Luccio, F., Pino, N. A., Piscini, A., & Ventura, G. (2015). Significance of the 1982–2014 Campi Flegrei seismicity: Preexisting structures, hydrothermal processes, and hazard assessment. *Geophysical Research Letters*, *42*(18), 7498–7506. https://doi.org/10.1002/2015gl064962

Di Martino, M. D. P., De Siena, L., Serlenga, V., & De Landro, G. (2022). Reconstructing hydrothermal fluid pathways and storage at the Solfatara crater (Campi Flegrei, Italy) using seismic scattering and absorption. *Frontiers in Earth Science*, *10*, 852510. https://doi.org/10.3389/feart.2022.852510

Fedele, A., Somma, R., Troise, C., Holmberg, K., De Natale, G., & Matano, F. (2020). Time-lapse landform monitoring in the Pisciarelli (Campi Flegrei-Italy) fumarole field using UAV photogrammetry. *Remote Sensing*, *13*(1), 118. https://doi.org/10.3390/rs13010118

Hainzl, S., Kraft, T., Wassermann, J., Igel, H., & Schmedes, E. (2006). Evidence for rainfall-triggered earthquake activity. *Geophysical Research Letters*, *33*(19), L19303. https://doi.org/10.1029/2006gl027642

Hannachi, A., Jolliffe, I. T., & Stephenson, D. B. (2007). Empirical orthogonal functions and related techniques in atmospheric science: A review. *International Journal of Climatology: A Journal of the Royal Meteorological Society*, *27*(9), 1119–1152. https://doi.org/10.1002/joc.1499

Isaia, R., Di Giuseppe, M. G., Troiano, A., Avino, R., Caliro, S., Santi, A., & Vitale, S. (2022). Structure and present state of the Astroni Volcano in the Campi Flegrei caldera in Italy based on multidisciplinary investigations. *Geochemistry, Geophysics, Geosystems*, *23*(12), e2022GC010534. https://doi.org/10.1029/2022gc010534

Isaia, R., Vitale, S., Di Giuseppe, M. G., Iannuzzi, E., Tramparulo, F. D. A., & Troiano, A. (2015). Stratigraphy, structure, and volcano-tectonic evolution of Solfatara maar-diatreme (Campi Flegrei, Italy). *GSA Bulletin*, *127*(9–10), 1485–1504. https://doi.org/10.1130/b31183.1

Kilburn, C. R., De Natale, G., & Carlino, S. (2017). Progressive approach to eruption at Campi Flegrei caldera in southern Italy. *Nature Communications*, *8*(1), 1–8. https://doi.org/10.1038/ncomms15312

Lomax, A., Michelini, A., & Curtis, A. (2014). Earthquake location, direct, global-search methods. In R. Meyers (Ed.), *Encyclopedia of complexity and systems science*. Springer. https://doi.org/10.1007/978-3-642-27737-5_150-2

Lorenz, E. N. (1956). *Empirical orthogonal functions and statistical weather prediction* (Vol. 1, p.52). Massachusetts Institute of Technology, Department of Meteorology.

Lu, S. M. (2018). A global review of enhanced geothermal system (EGS). *Renewable and Sustainable Energy Reviews*, *81*, 2902–2921. https://doi.org/10.1016/j.rser.2017.06.097

Matthews, A. J., Barclay, J., & Johnstone, J. E. (2009). The fast response of volcano-seismic activity to intense precipitation: Triggering of primary volcanic activity by rainfall at Soufrière Hills volcano, Montserrat. *Journal of Volcanology and Geothermal Research*, *184*(3–4), 405–415. https://doi.org/10.1016/j.jvolgeores.2009.05.010

Monahan, A. H., Fyfe, J. C., Ambaum, M. H., Stephenson, D. B., & North, G. R. (2009). Empirical orthogonal functions: The medium is the message. *Journal of Climate*, *22*(24), 6501–6514. https://doi.org/10.1175/2009jcli3062.1

Moretti, R., Troise, C., Sarno, F., & De Natale, G. (2018). Caldera unrest driven by CO_2-induced drying of the deep hydrothermal system. *Scientific Reports*, *8*(1), 1–11. https://doi.org/10.1038/s41598-018-26610-2

Navarra, A., & Simoncini, V. (2010). *A guide to empirical orthogonal functions for climate data analysis*. Springer Science & Business Media.

Nespoli, M., Belardinelli, M. E., & Bonafede, M. (2021). Stress and deformation induced in layered media by cylindrical thermo-poroelastic sources: An application to Campi Flegrei (Italy). *Journal of Volcanology and Geothermal Research*, *415*, 107269. https://doi.org/10.1016/j.jvolgeores.2021.107269

Neuberg, J. (2000). External modulation of volcanic activity. *Geophysical Journal International*, *142*(1), 232–240. https://doi.org/10.1046/j.1365-246x.2000.00161.x

Pepe, S., De Siena, L., Barone, A., Castaldo, R., D'Auria, L., Manzo, M., et al. (2019). Volcanic structures investigation through SAR and seismic interferometric methods: The 2011–2013 Campi Flegrei unrest episode. *Remote Sensing of Environment*, *234*, 111440. https://doi.org/10.1016/j.rse.2019.111440

Petrosino, S., Cusano, P., & Madonia, P. (2018). Tidal and hydrological periodicities of seismicity reveal new risk scenarios at Campi Flegrei caldera. *Scientific Reports*, *8*(1), 1–12. https://doi.org/10.1038/s41598-018-31760-4

Petrosino, S., & De Siena, L. (2021). Fluid migrations and volcanic earthquakes from depolarized ambient noise. *Nature Communications*, *12*(1), 1–8. https://doi.org/10.1038/s41467-021-26954-w

Petrosino, S., & Dumont, S. (2022). Tidal modulation of hydrothermal tremor: Examples from Ischia and Campi Flegrei volcanoes, Italy. *Frontiers in Earth Science*, *9*, 775269. https://doi.org/10.3389/feart.2021.775269

Petrosino, S., Ricco, C., & Aquino, I. (2021). Modulation of ground deformation and earthquakes by rainfall at Vesuvius and Campi Flegrei (Italy). *Frontiers in Earth Science*, *9*, 758602. https://doi.org/10.3389/feart.2021.758602

Roman, D. C., & Cashman, K. V. (2018). Top–down precursory volcanic seismicity: Implications for 'stealth' magma ascent and long-term eruption forecasting. *Frontiers in Earth Science*, *6*, 124. https://doi.org/10.3389/feart.2018.00124

Scafetta, N., & Mazzarella, A. (2021). On the rainfall triggering of Phlegraean Fields volcanic tremors. *Water*, *13*(2), 154. https://doi.org/10.3390/w13020154

Siniscalchi, A., Tripaldi, S., Romano, G., Chiodini, G., Improta, L., Petrillo, Z., et al. (2019). Reservoir structure and hydraulic properties of the Campi Flegrei geothermal system inferred by audiomagnetotelluric, geochemical, and seismicity study. *Journal of Geophysical Research: Solid Earth*, *124*(6), 5336–5356. https://doi.org/10.1029/2018jb016514

Smith, T. M., Reynolds, R. W., Livezey, R. E., & Stokes, D. C. (1996). Reconstruction of historical sea surface temperatures using empirical orthogonal functions. *Journal of Climate*, *9*(6), 1403–1420. https://doi.org/10.1175/1520-0442(1996)009<1403:rohsst>2.0.co;2

Thiiébaux, H. J., & Zwiers, F. W. (1984). The interpretation and estimation of effective sample sizes. *Journal of Climate and Applied Meteorology*, *23*(5), 800–811. https://doi.org/10.1175/1520-0450(1984)023<0800:tiaeoe>2.0.co;2

Tramelli, A., Giudicepietro, F., Ricciolino, P., & Chiodini, G. (2022). The seismicity of Campi Flegrei in the contest of an evolving long term unrest. *Scientific Reports*, *12*(1), 1–12. https://doi.org/10.1038/s41598-022-06928-8

Tramelli, A., Godano, C., Ricciolino, P., Giudicepietro, F., Caliro, S., Orazi, M., & Chiodini, G. (2021). Statistics of seismicity to investigate the Campi Flegrei caldera unrest. *Scientific Reports*, *11*(1), 1–10. https://doi.org/10.1038/s41598-021-86506-6

Vanorio, T., & Kanitpanyacharoen, W. (2015). Rock physics of fibrous rocks akin to Roman concrete explains uplifts at Campi Flegrei Caldera. *Science*, *349*(6248), 617–621. https://doi.org/10.1126/science.aab1292

Vanorio, T., Virieux, J., Capuano, P., & Russo, G. (2005). Three-dimensional seismic tomography from P wave and S wave microearthquake travel times and rock physics characterization of the Campi Flegrei Caldera. *Journal of Geophysical Research*, *110*(B3), B03201. https://doi.org/10.1029/2004jb003102

Vilardo, G., Isaia, R., Ventura, G., De Martino, P., & Terranova, C. (2007). InSAR Permanent Scatterer analysis reveals fault re-activation during inflation and deflation episodes at Campi Flegrei caldera. *Remote Sensing of Environment*, *114*(10), 2373–2383. https://doi.org/10.1016/j.rse.2010.05.014

Zerbini, S., Raicich, F., Errico, M., & Cappello, G. (2013). An EOF and SVD analysis of interannual variability of GPS coordinates, environmental parameters and space gravity data. *Journal of Geodynamics*, *67*, 111–124. https://doi.org/10.1016/j.jog.2012.04.006